Stephan Ulmer
Olav Jansen *Editors*

fMRI

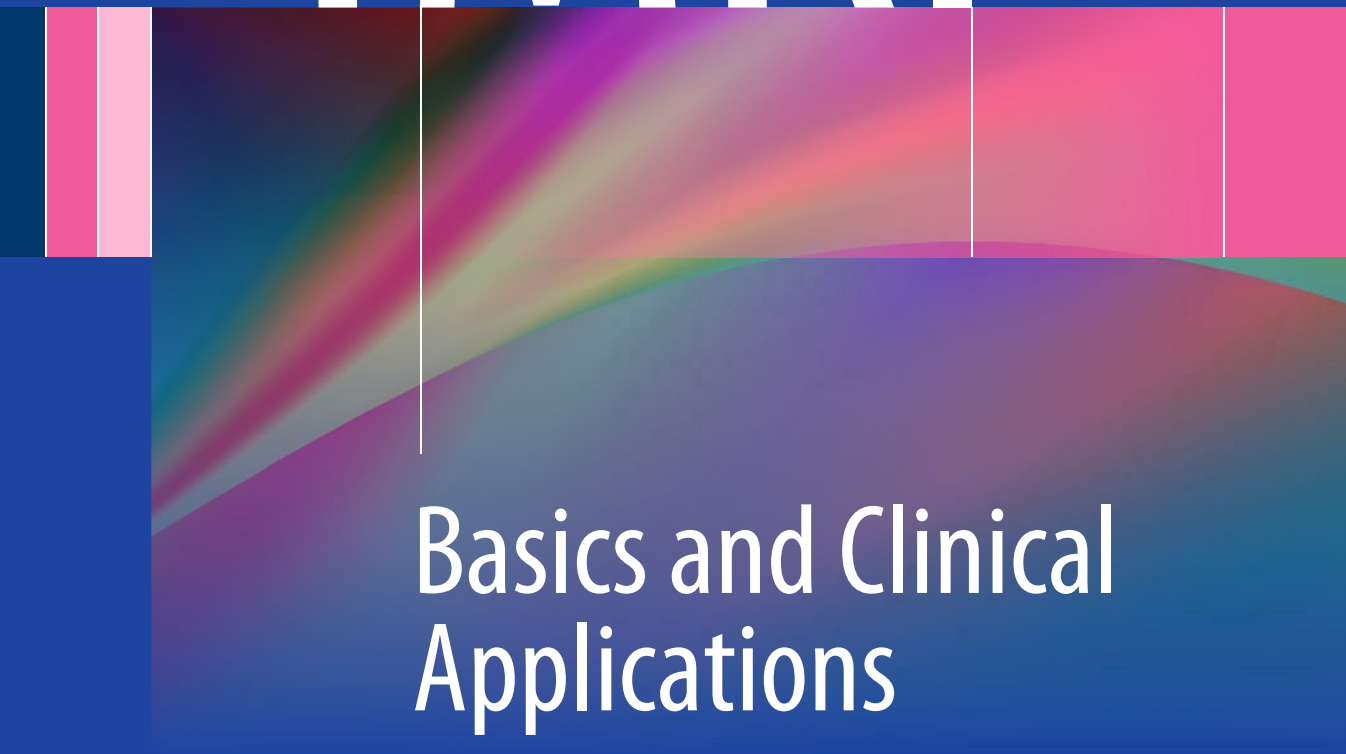

Basics and Clinical Applications

Second Edition

Springer

fMRI

Stephan Ulmer • Olav Jansen
Editors

fMRI

Basics and Clinical Applications

Second Edition

Springer

Editors
Stephan Ulmer
Medizinisch Radiologisches Institut
(MRI) Zürich
(Bahnhofsplatz/Bethanien/Stadelhofen)
Zürich
Switzerland

Olav Jansen
Institut für Neuroradiologie
Universitätsklinikum Schleswig-Holstein
Kiel
Germany

Institut für Neuroradiologie
Universitätsklinikum Schleswig-Holstein
Kiel
Germany

ISBN 978-3-642-34341-4 ISBN 978-3-642-34342-1 (eBook)
DOI 10.1007/978-3-642-34342-1
Springer Heidelberg New York Dordrecht London

Library of Congress Control Number: 2013935476

Contents

Part I Basics

1 Introduction 3
Stephan Ulmer

2 Neuroanatomy and Cortical Landmarks 7
Stephan Ulmer

3 Spatial Resolution of fMRI Techniques 17
Seong-Gi Kim, Tao Jin, and Mitsuhiro Fukuda

4 The Electrophysiological Background of the fMRI Signal 25
Christoph Kayser and Nikos K. Logothetis

5 High-Field fMRI 37
Elke R. Gizewski

6 fMRI Data Analysis Using SPM 51
Guillaume Flandin and Marianne J.U. Novak

7 Meta-Analyses in Basic and Clinical Neuroscience: State of the Art and Perspective 77
Simon B. Eickhoff and Danilo Bzdok

Part II Clinical Applications

8 Preoperative Blood Oxygen Level-Dependent (BOLD) Functional Magnetic Resonance Imaging (fMRI) of Motor and Somatosensory Function 91
Christoph Stippich

9 The Functional Anatomy of Speech Processing: From Auditory Cortex to Speech Recognition and Speech Production 111
Gregory Hickok

10 Use of fMRI Language Lateralization for Quantitative Prediction of Naming and Verbal Memory Outcome in Left Temporal Lobe Epilepsy Surgery 119
Jeffrey R. Binder

11 Mapping of Recovery from Poststroke Aphasia: Comparison of PET and fMRI 141
Wolf-Dieter Heiss

12 Functional Magnetic Resonance-Guided Brain Tumor Resection 155
Peter D. Kim, Charles L. Truwit, and Walter A. Hall

13 Direct Cortical Stimulation and fMRI 169
H. Maximillian Mehdorn, Simone Goebel, and Arya Nabavi

14 Imaging Epilepsy and Epileptic Seizures Using fMRI 177
Simon M. Glynn and John A. Detre

15 Multimodal Brain Mapping in Patients with Early Brain Lesions 191
Martin Staudt

16 Special Issues in fMRI Involving Children 197
Lucie Hertz-Pannier and Marion Noulhiane

17 Modeling Connectivity in Health and Disease: Examples from the Motor System 213
Simon B. Eickhoff and Christian Grefkes

18 fMRI in Parkinson's Disease 227
Hartwig R. Siebner and Damian M. Herz

19 The Perirhinal, Entorhinal, and Parahippocampal Cortices and Hippocampus: An Overview of Functional Anatomy and Protocol for Their Segmentation in MR Images 239
Sasa L. Kivisaari, Alphonse Probst, and Kirsten I. Taylor

20 Simultaneous EEG and fMRI Recordings (EEG-fMRI) 269
Friederike Moeller, Michael Siniatchkin, and Jean Gotman

21 Combining Transcranial Magnetic Stimulation with (f)MRI 283
Gesa Hartwigsen, Tanja Kassuba, and Hartwig R. Siebner

22 Clinical Magnetoencephalography and fMRI 299
Steven M. Stufflebeam

23 Incidental Findings in Neuroimaging Research: Ethical Considerations 311
Stephan Ulmer, Thomas C. Booth, Guy Widdershoven, Olav Jansen, Gunther Fesl, Rüdiger von Kummer, and Stella Reiter-Theil

Index 319

Part I

Basics

Introduction

1

Stephan Ulmer

Within the past two decades, functional magnetic resonance imaging (fMRI) has developed tremendously and continues to do so. From initial descriptions of changes in blood oxygenation that can be mapped with MRI using T2*-weighted images to very basic investigations performing studies of the visual and motor cortex, fMRI has further evolved into a very powerful research tool and has also become an imaging modality of daily clinical routine, especially for presurgical mapping. With the first edition of this book, we tried to give an overview of the basic concepts and their clinical applications. With increasing demands by you, the reader, as a researcher and/or clinical colleague, and due to increasing applications, we feel an update is due, with add-ons to the previous edition. We are delighted to present this second edition of *fMRI: Basics and Clinic Applications*.

Understanding brain function and localizing functional areas have ever since been a main goal of neuroscience, with fMRI being a very powerful tool to approach this aim. Studies on healthy volunteers usually take a different approach and often have a very complex study design, while clinical applications face other problems most commonly related to the limited compliance of the patients, even more so in the context of dementia, advanced-stage tumor patients, or with children. Therefore, the application of fMRI in a clinical setting is a different challenge, reflected in the study designs as well as in the analysis of the data algorithms. Analyzing data also has become increasingly complex due to sophisticated study designs in single-center studies, multicenter trials requiring meta-analysis, and for mapping connectivity. Analyzing fMRI data is a science of its own. Fortunately, there is a variety of software solutions available free of charge for the most part. Manufacturers also offer analyzing software.

Besides the classical definition of functional areas that might have been shifted through a lesion or could be present in a distorted anatomy prior to neurosurgical resection, further clinical applications include mapping of recovery from stroke or trauma, cortical reorganization (if these areas were affected), and changes during the development of the brain or during the course of a disease. For the understanding of psychiatric disorders, dementia, and Parkinson's disease, fMRI offers new horizons.

Knowledge of basic neuroanatomy, the associated physiology, and especially the possible pathophysiology that might affect the results to start with is mandatory. The results in volunteers are the requisite to understand the results in patients, and they can only be as good as the design itself. Monitoring the patient in the scanner is necessary to guarantee that the results obtained

S. Ulmer
Medizinisch Radiologisches Institut (MRI) Zürich, (Bahnhofsplatz/Bethanien/Stadelhofen), Bahnhofsplatz 3, Zürich 8001, Switzerland

Institut für Neuroradiologie, Universitätsklinikum Schleswig-Holstein, Schittenhelmstrasse 10, Kiel 24105, Germany
e-mail: ulmer@email.com

S. Ulmer, O. Jansen (eds.), *fMRI – Basics and Clinical Applications*,
DOI 10.1007/978-3-642-34342-1_1,

will reflect activation caused by the stimulation, or to understand that reduced or even missing activation could have hampered the results, and to analyze how they were generated. Obviously, we have to realize that while the patient is still in the scanner, a repetition of the measurement can be done or an unnecessary scan avoided if the patient is incapable of performing the task. Performing motor tasks seems relatively straightforward, as patient performance can be directly observed in the scanner. Cognitive and language tasks are more challenging. Also, a vascular stenosis or the steal effects of a brain tumor or an arteriovenous malformation (AVM) may corrupt the results. There are some sources resulting in disturbances that might depict no activation in a patient, e.g., in language tasks that usually depict reliable results in volunteers. It is essential to have a person with expertise in training and testing patients on the cognitive tasks involved, such as a neuropsychologist or a cognitive neurologist.

Task performance and paradigm development usually follow a graduated scheme. Initially, experiments are performed in healthy volunteers. This, however, has the disadvantage that the volunteers are most likely healthy students or staff who are used to the scanner environment and can therefore focus unrestrictedly on the task, whereas patients may be scared or too nervous concerning their disease and about what might happen in the near future (such as a brain tumor resection).

The same paradigm must be used in less affected patients first, to confirm the feasibility in this setting that might become more specific after some experience. Test-retest reliability finally enables clinical application to address specific questions. Passive or "covert" tasks might be helpful; however, at least in cognitive studies performance cannot be measured. Semantic and cognitive processes continue during passive situations, including rest and other passive baseline conditions. Regions involved will therefore be eliminated from the analysis when such conditions are used as a baseline.

Mapping children represents a twofold challenge. Normative data is not available and compliance is limited. In early childhood or in cognitively impaired children, or just simply during brain development, cognitive tasks need to be modified individually, and that again causes problems in analyzing the data and interpreting the results.

As already stated, absence of an expected activation represents a real challenge and raises the question of the reliability of the method per se. Suppression of activation or task-related signal intensity decrease has also not been fully understood. Missing activation in a language task could mislead the neurosurgeon to resect a low-grade lesion close to the inferior frontal lobe and still cause speech disturbance or memory loss after resection of a lesion close to the mesial temporal lobe, and therefore – depending on the close cooperation between the clinicians – healthy skepticism as well as combination with other modalities such as direct cortical stimulation may be advisory. Indeed, the combination of fMRI with further modalities such as electroencephalography (EEG), transcranial magnetic stimulation (TMS), magnetoencephalography (MEG), or positron emission tomography (PET) is very promising. Hemispheric (language) dominance is only the tip of the iceberg and we have to ask ourselves again how sensitive our methods and paradigms are to depict minor deficits. The same is true for clinical bedside testing and thus questions "silent" brain regions.

Sequence selection is important in terms of what we want to see and how to achieve it. Prior to the introduction of echo planar imaging, temporal resolution was restricted. Spatial resolution requirements are much more important in individual cases than in a healthy control group, especially in the presurgical definition of the so-called eloquent areas.

Higher field strengths might enable us to depict more signals but possibly more noise in the data as well. From a clinician's point of view, reliability of individual results is desired.

It is exciting to see how fMRI became a clinical application in recent years of which neurosurgeons were initially very suspicious during the first clinical experiments in presurgical mapping. Its current acceptance can be appreciated in the increasing numbers of studies performed on demand, not only in brain tumor mapping but also in epilepsy.

A completely new field has developed more recently, namely, ethical considerations arising from incidental imaging findings. For patients, incidental findings are often part of the daily routine, yet "healthy" volunteers are faced with completely unexpected consequences and so are researchers.

With the second edition of this book, we will try to answer new questions while giving an overview on how fMRI can be applied for clinical purposes. After the first edition we felt the need to add further fields and applications, this being an ongoing project that we try to keep alive. It is a great honor for me to have such a distinguished board of experts in the field involved in this project. I hope that you will enjoy this book as much as I have and that it will help you in your own daily work.

Neuroanatomy and Cortical Landmarks

2

Stephan Ulmer

2.1 Neuroanatomy and Cortical Landmarks of Functional Areas

Prior to any type of functional mapping, a profound knowledge of neuroanatomy is mandatory. Focusing on the clinical applications of fMRI, this chapter will present methods to identify characteristic anatomical landmarks and describe the course and shape of some gyri and sulci and how they can be recognized on MR imaging. As anatomy will be presented in neurofunctional systems, some redundancy is desired in order to course over cortical landmarks. If fMRI is not performed during clinical routine imaging, usually a 3D data set is acquired to overlay the results. Nowadays, fMRI is performed using echo planar imaging (EPI) with anisotropic distortion, whereas 3D T1-weighted data sets, such as MPRage (magnetization-prepared rapid acquisition gradient echo) or SPGR (spoiled gradient-recalled acquisition in steady state) sequences, are usually isotropic. Normalization of the fMRI data may reduce this systemic error to some extent that is more pronounced at the very frontal aspect of the frontal lobe and the very posterior aspect of the occipital lobe. However, for individual data, normalization and overlaying fMRI results on anatomy remain crucial. No two brains, not even the two hemispheres within one subject, are identical at a macroscopic level, and anatomical templates represent only a compromise (Devlin and Poldrack 2007). Usage of templates like the Talairach space (based on the anatomy of one brain) or the MNI template (based on 305 brains) can cause registration error as well as additional variation and reduce accuracy; indeed, it does not warrant the shammed anatomical precision in the individual case.

S. Ulmer
Medizinisch Radiologisches Institut (MRI) Zürich, (Bahnhofsplatz/Bethanien/Stadelhofen), Bahnhofsplatz 3, Zürich 8001, Switzerland

Institut für Neuroradiologie, Universitätsklinikum Schleswig-Holstein, Schittenhelmstrasse 10, Kiel 24105, Germany
e-mail: ulmer@email.com

2.1.1 Sensorimotor Cortex

2.1.1.1 Transverse Sections

There are various methods to identify the precentral gyrus (preCG; [3]), the central sulcus (CS) and the postcentral gyrus (postCG; [4]). From a craniocaudal point of view, the sensorimotor strip follows (from the apex to the Sylvian fissure [35b]) a medial-posterior-superior to lateral-anterior-inferior course. The precentral gyrus [3] fuses with the superior frontal gyrus (SFG; [1]) at the very upper convexity (Ebeling et al. 1986; Kido et al. 1980; Naidich et al. 1995; Ono et al. 1990). This can be well depicted on transverse sections (see Figs. 2.1 and 2.2). The precentral gyrus [3] is the most posterior part of the frontal lobe that extends inferiorly to the Sylvian fissure [35b]. The precentral gyrus [3] is thicker than the postcentral gyrus [4] in anterior-posterior (ap) dimension (Naidich et al. 1995) as is the grey

S. Ulmer, O. Jansen (eds.), *fMRI – Basics and Clinical Applications*,
DOI 10.1007/978-3-642-34342-1_2,

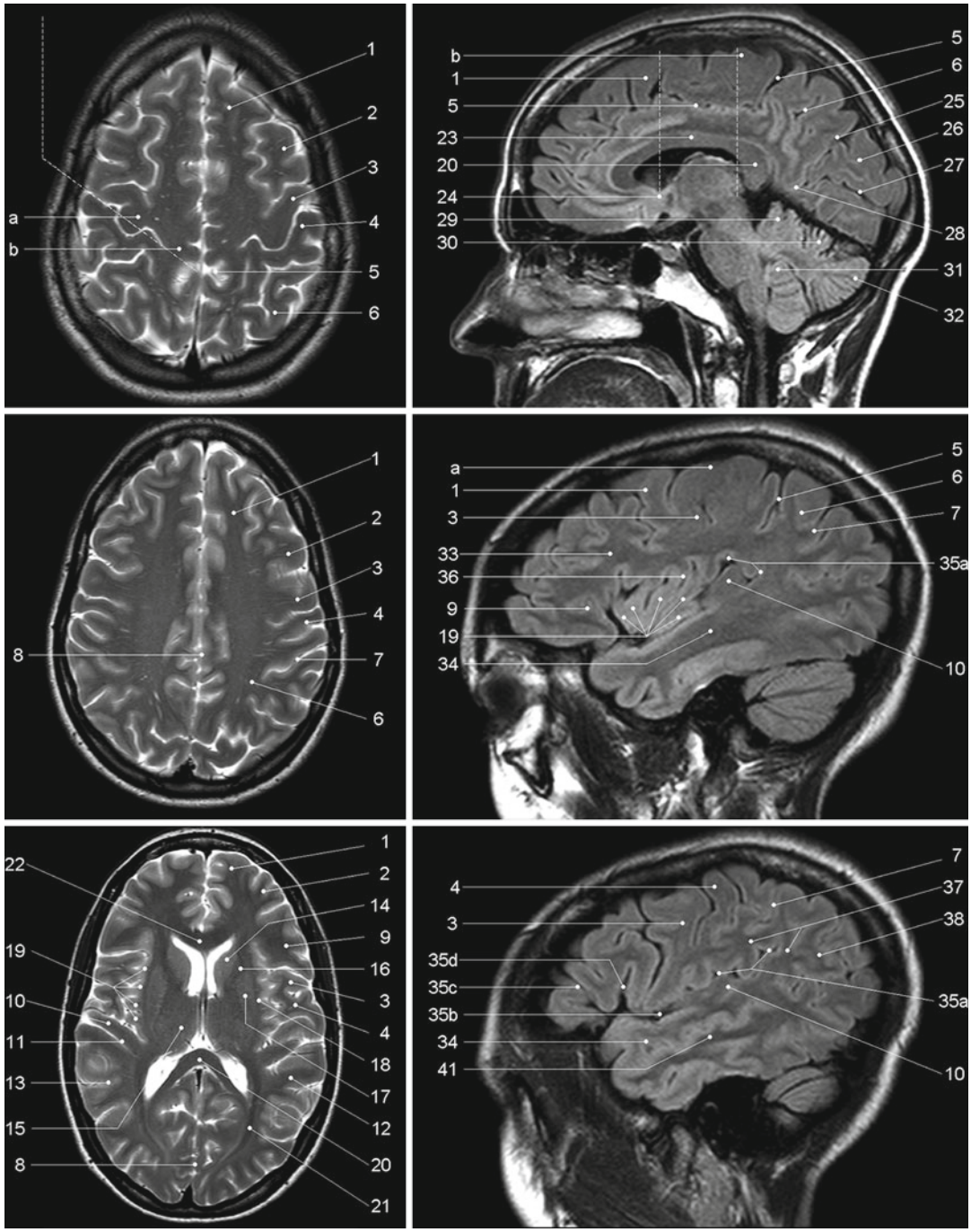

Fig. 2.1 Overview of the used sections. The numbers are explained within the text as well as in the other figure legends in detail

matter (Meyer et al. 1996). At the apex, the pre- [3] and postcentral gyri [4] form the paracentral lobule [b] as they fuse. Making a little detour to a lateral view (see Fig. 2.3), the cingulate sulcus [5] ascends at the medial interhemispheric surface dorsal to the paracentral lobule (pars marginalis)

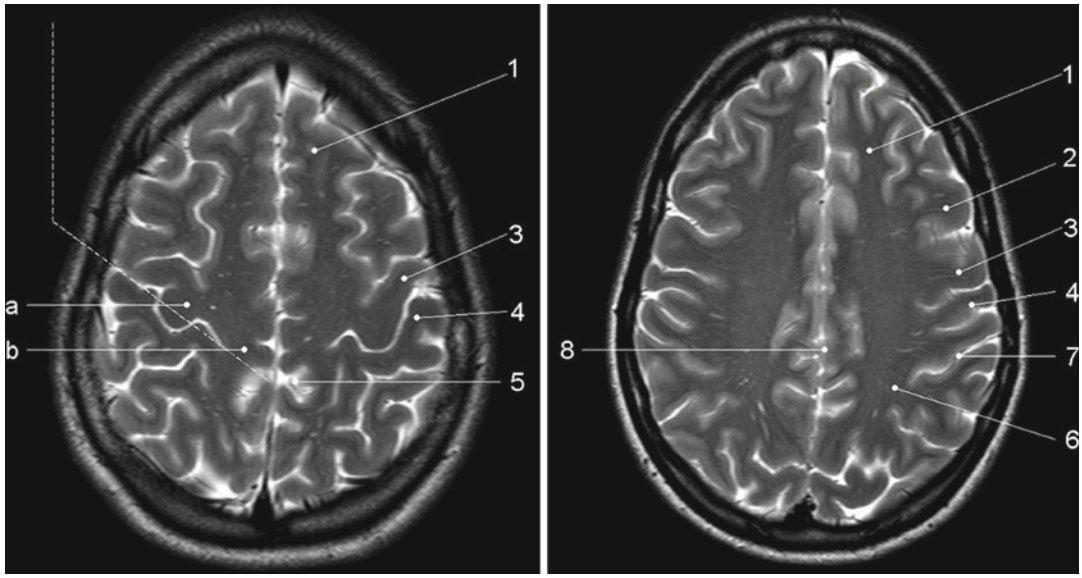

Fig. 2.2 Axial T2-weighted TSE MR images. *1* superior frontal gyrus, *2* medial frontal gyrus, *3* precentral gyrus, *4* postcentral gyrus, *5* "pars bracket", cingulated sulcus, *6* precuneus, parietal lobe, *7* intraparietal sulcus, *8* interhemispheric fissure, *a* hand knob, *b* paracentral lobule

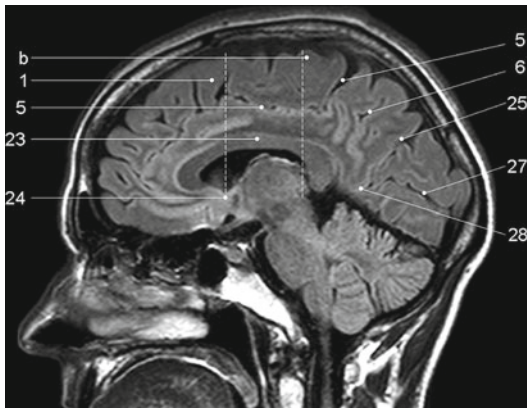

Fig. 2.3 Sagittal FLAIR image at the midline. *1* superior frontal gyrus, *5* "pars bracket", cingulate sulcus, *6* precuneus, parietal lobe, *23* body of the corpus callosum, *24* anterior commissure, *25* parietooccipital sulcus, *27* calcarine fissure, *b* paracentral lobule, *28* cuneal point

[b] and thus separates it from the precuneus [6]. This intersection can be appreciated on axial sections as the "bracket" sign (see Fig. 2.2; Naidich and Brightbill 1996) that borders the postcentral gyrus [4]. Somatotopographically, the apex harbours the cortical representation the lower extremity (Penfield and Rasmussen 1950). Following its course along the superficial convexity (from medial-posterior-superior to lateral-anterior-inferior), the cortical surface of the precentral gyrus increases at its posterior margin, building the omega-shaped motor hand knob ([a]; Yousry et al. 1995, 1997). Within this primary motor cortex (M1) of the hand, there is an additional somatotopic order of the individual digits (with interindividual overlap and variation). From medial to lateral, the hand is organized beginning with digit 5 (D5), to the thumb representation (D1) being the most lateral (Dechent and Frahm 2003). The motor hand knob [a] is another typical landmark of the precentral gyrus [3]; however, as the CS and the postcentral gyrus [4] follow this course, there is also an omega-shaped structure in the postcentral gyrus (harbouring the somatosensory hand area). However, as described above, the ap-dimension of the postcentral gyrus [4] is smaller compared to the precentral gyrus [3], thus often enabling a differentiation. Somatotopographically, the cortical somatosensory representation follows the distribution of the precentral gyrus [3] (Penfield and Rasmussen 1950; Overduin and Servos 2004). Lateral to the SFG [1], the medial frontal gyrus [2] zigzags posteriorly and points towards the motor

hand knob [a]. Beginning at this "junction" and lateral-inferior to this landmark, the ap-diameter of the preCG [3] decreases, but it increases again along the lower convexity. This has already been recognized by Eberstaller (1890). Using modern imaging techniques, the diameter had been measured and the previous findings validated that the biggest diameter of the preCG [3] is found at the lower portion of the gyrus adjacent to the Sylvian fissure [35b] (Ono et al. 1990). This is the primary motor cortex (M1) of lip representation and tongue movements. In the axial sections, there is neither a typical shape or landmark of the gyrus, nor does measuring from the motor hand area or the ac (anterior commissure) help us to describe the location precisely. This can be solved on sagittal sections (see below).

Previously, the anatomy of the frontal lobe has been described partially. As the course of the medial frontal gyrus [2] can be followed nicely on axial sections, the lateral inferior aspect of the frontal lobe represents the inferior frontal gyrus. Anterior to the preCG [3], the prefrontal motor areas can be found. The inferior frontal gyrus borders and overhangs the insula [19] anteriorly. This part is the frontal operculum [9] harbouring the motor speech area of Broca (see below sagittal sections).The lateral ventricles with its anterior and posterior horn can easily be depicted on axial sections due to its typical form and typical signal caused by corticospinal fluid (CSF, see Figs. 2.1, 2.5 and 2.6). Their shape is formed through the head of the caudate nucleus [10] lateral to the anterior horn, the thalamus [11] lateral at its waist (III. ventricle) and posteriorly by the fibres of the anterior-posteriorly running optic radiation [21] and left-right running fibres of the splenium [20] (see Figs. 2.5 and 2.6). Lateral to these structures, descending corticospinal fibres pass the internal capsule [16] and follow a certain somatotopic organization. The internal capsule is framed medial by the head of the caudate nucleus [10], the third ventricle and the thalamus [11] (at the posterior aspect of the third ventricle) and lateral by the globus pallidus [17]. From medial to lateral towards the insula [19], the globus pallidus, putamen and claustrum within the lentiform nucleus [17] can be differentiated. In the anterior limb and the genu of the internal capsule, [16] corticospinal fibres from the tongue, lip and face descend, whereas in the posterior limb, fibres from the upper extremity, body and finally lower extremity are found.

2.1.1.2 Sagittal Sections

Previously sagittal sections have been described at the interhemispheric surface (see Fig. 2.3). The corpus callosum [20, 22, 23] represents the biggest connection between the two hemispheres. The frontal aspect is the genu [22], the medial part is the body [23] and the most rostral part is the splenium [20]. The corpus callosum encases the lateral ventricles. At the base, the anterior commissure (ac; [24]) can be identified as a roundish structure. Sometimes, the posterior commissure (pc) can also be defined, which represents a bundle of white fibres crossing the midline, at the dorsal aspect of the upper end of the cerebral aqueduct. Previously slice orientation of most fMRI studies had been performed according to this ac-pc line in order to have a reference system.

From the base to the apex, the corpus callosum is abutted by the callosal sulcus and the cingulate gyrus. The gyrus abutting the cingulate sulcus [5] is the medial part of the SFG [1]. In the region (at the medial cortical surface) framed by vertical lines perpendicular to the ac (Vac) or pc (Vpc; see Fig. 2.3), the supplementary motor area (SMA) is harboured in the cingulate gyrus and superior frontal gyrus. As described above, the cingulate sulcus [5] ascends at the medial interhemispheric surface (see Fig. 2.3) dorsal to the paracentral lobule ([b]; pars marginalis) and thus separates it from the precuneus [6]. This intersection can be nicely appreciated on axial sections as the "bracket" sign (see Fig. 2.2; Naidich and Brightbill 1996) that borders the postcentral gyrus [4]. The postcentral gyrus is already a part of the parietal lobe. The precuneus [6] is located dorsal to the postcentral sulcus. There is another important landmark that separates the parietal lobe from the occipital lobe (cuneus [26]), the parietooccipital sulcus [25]. It can be easy recognized in sagittal views (see Fig. 2.3), as the dorsal sulcus that follows an inferior-anterior to superior-posterior course, posterior to the ascending

part of the cingulate sulcus [5]. It is advisable to follow one of these structures moving laterally through the brain in sagittal sections. Once the Sylvian fissure [35b] can be identified, anatomical landmarks are again easy to define.

In midsagittal sections (see Fig. 2.6), the motor hand knob [a] can again be recognized as a "hook" that rises out of the parenchyma and points dorsally. Further, laterally the sensorimotor cortex overhangs the insula [19]. The Sylvian fissure [35b] that separates the frontal lobe and the temporal lobe has an inferior-anterior to superior-posterior course. At its anterior margin, it ascends into the anterior horizontal ramus [35c] and more dorsally into the anterior ascending ramus [35d] of the frontal operculum [9] that also overhangs the anterior aspect of the insula [19]. The anterior horizontal ramus [35c] separates the pars orbitalis [40] from the pars triangularis [39], whereas the anterior ascending ramus [35d] separates the pars triangularis [39] from the pars opercularis [9] of the frontal operculum of the inferior frontal gyrus and thus forms an "M" (Naidich et al. 1995). The pars opercularis [9] of the frontal operculum of the inferior frontal lobe harbours Broca's area. At its posterior margin, the pars opercularis is delimited by the anterior subcentral sulcus. At the base of the sensorimotor strip, the precentral [3] and postcentral gyrus [4] fuse (Eberstaller 1890; Ono et al. 1990). This junction is delimited dorsally by the posterior subcentral sulcus. Movement of the lips or tongue induce an increase in BOLD signal at this portion (Fesl et al. 2003, own observations). The base of the sensorimotor area has, depending on anatomical variations, a "K" or an "N" shape that is built by the anterior subcentral sulcus and inferior precentral sulcus, the precentral gyrus, posterior subcentral sulcus, postcentral gyrus and postcentral sulcus that again borders the angular gyrus [38] (Eberstaller 1890; Ono et al. 1990, own observations; see Fig. 2.6). The posterior part of the Sylvian fissure separates – following its superior-posterior course – and ascends into the posterior ascending ramus [35a] flanked by the anterior and posterior aspect of the supramarginal gyrus [37] that has a horseshoe appearance.

2.1.2 The Insula

The insula [19] is covered by the superior temporal gyrus [34], the frontal operculum [9] and the base of the sensorimotor strip. Its anatomy is best depicted in sagittal sections (see Fig. 2.6).

2.1.2.1 Sagittal Sections

The insula [19] is separated by the CS [36] that runs from superior-posterior towards the inferior-anterior located apex of the insula into an anterior lobule and a posterior lobule (see Fig. 2.6). The anterior lobule consists of three gyri (anterior, medial and posterior short insular gyri); the posterior lobule consists of two gyri, the anterior long insular gyrus and the posterior long insular gyrus separated by the postcentral gyrus (Naidich et al. 2004).

From a neurofunctional point of view, the insula has various functional areas. The anterior lobule was found to cause word-finding difficulties during electrical stimulation in epilepsy surgery (Ojemann and Whitaker 1978a, b) and to be responsible for speech planning (Wise et al. 1999; Price 2000). Speech apraxia is induced through lesions in the left precentral gyrus of the insula (Dronkers 1996; Nagao et al. 1999), whereas the right anterior lobule becomes activated during vocal repetition of nonlyrical tunes (Riecker et al. 2000). Stimulation of the right insula increases sympathetic tone, and stimulation of the left insula increases parasympathetic tone (Oppenheimer 1993), possibly playing a role in cardiac mortality in left insular stroke. Finally visual-vestibular interactions have been found (Brandt et al. 1998) to name a few systems.

2.1.2.2 Transverse Sections

The insular cortex [19] is delimited medially by the globus pallidus, putamen and claustrum (lentiform nucleus [17]) and separated by a small border of white matter (extreme capsula [18]). The gyri can be differentiated by counting each knob starting ventrally at the anterior peri-insular sulcus that abuts the pars opercularis [9] of the frontal operculum of the inferior frontal gyrus (see Figs. 2.4 and 2.5). Five knobs can be defined (anterior, medial and posterior short insular gyri and anterior and posterior long insular gyri).

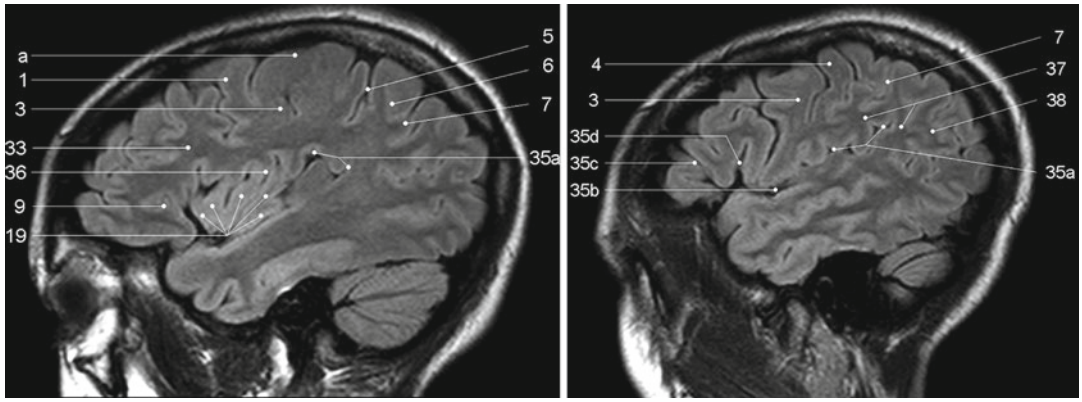

Fig. 2.4 Sagittal FLAIR images. *1* superior frontal gyrus, *3* precentral gyrus, *4* postcentral gyrus, *5* "pars bracket", cingulate sulcus, *6* precuneus, parietal lobe, *7* intraparietal sulcus, *9* pars opercularis, inferior frontal lobe, frontal operculum, *19* insula (anterior and posterior short insular gyri, anterior and posterior long insular gyri), *33* medial frontal gyrus, *35a* posterior ascending ramus of the Sylvian fissure, *35b* Sylvian fissure, *35c* anterior horizontal ramus of the Sylvian fissure, *35d* anterior ascending ramus of the Sylvian fissure, *36* central sulcus of the insula, *37* supramarginal gyrus, *38* angular gyrus, *a* hand knob

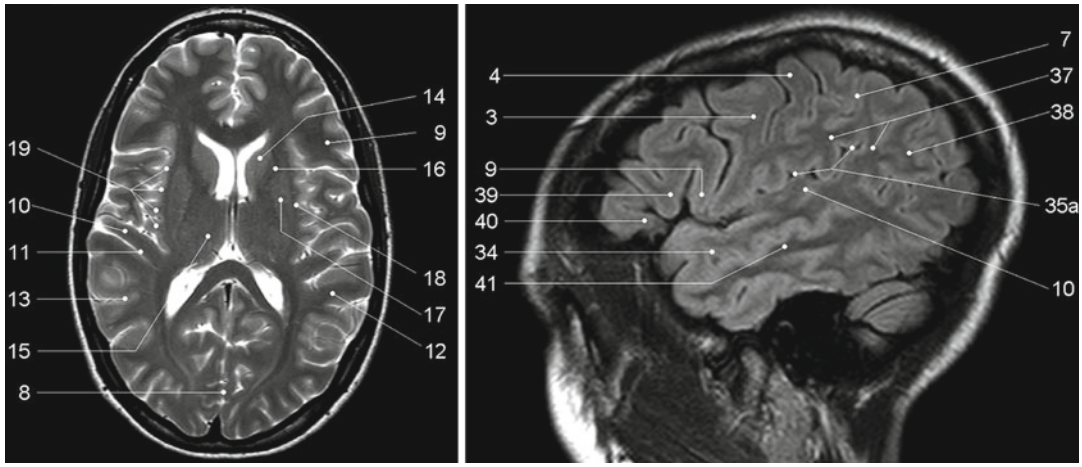

Fig. 2.5 Axial T2-weighted TSE MR and sagittal FLAIR images. *3* precentral gyrus, *4* postcentral gyrus, *7* intraparietal sulcus, *8* interhemispheric fissure, *9* pars opercularis, inferior frontal lobe, frontal operculum, *10* Heschl's gyrus, *11* Heschl's sulcus, *12* planum temporale, *13* superior temporal sulcus, *14* head of the caudate nucleus, *15* thalamus, *16* internal capsule, *17* globus pallidus, putamen, claustrum (lentiform nucleus), *18* extreme capsule, *19* insula (anterior and posterior short insular gyri, anterior and posterior long insular gyri), *34* superior temporal gyrus, *35a* posterior ascending ramus of the Sylvian fissure, *37* supramarginal gyrus, *38* angular gyrus, *39* pars triangularis, frontal operculum, inferior frontal gyrus, *40* pars orbitalis, frontal operculum, inferior frontal gyrus, *41* medial temporal gyrus

2.1.3 Speech-Associated Frontal Areas

2.1.3.1 Transverse Sections

In axial sections, the insula [19] can be found easily (see Figs. 2.5 and 2.6). From medial (ventricles) to lateral, the globus pallidus, putamen and claustrum, within the lentiform nucleus, [17] can be differentiated followed by the extreme capsula [18] and the cortex of the insula [19]. The Sylvian fissure [35b] separates the insula [19] from the temporal lobe. As stated above, the insula – taking anatomic variations into account – has 4–5 knobs

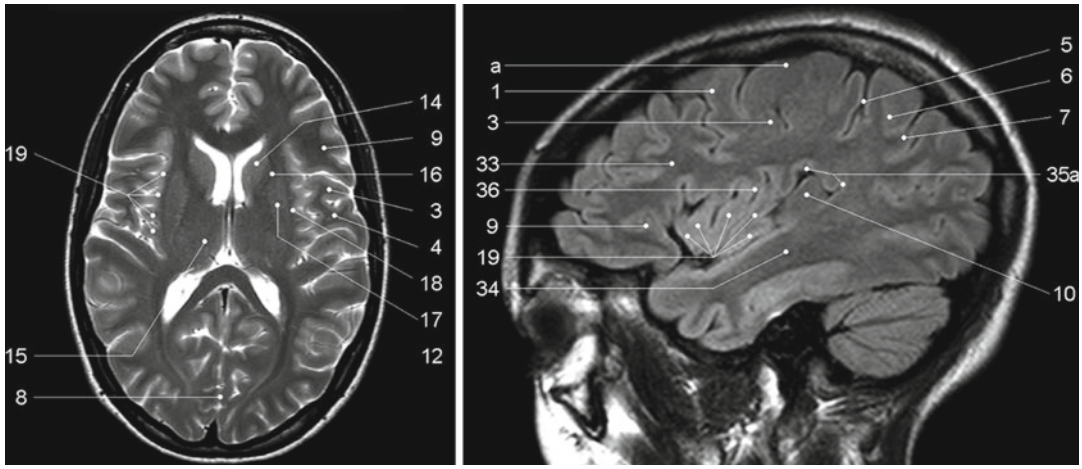

Fig. 2.6 Axial T2-weighted TSE MR and sagittal FLAIR images. *1* superior frontal gyrus, *3* precentral gyrus, *4* postcentral gyrus, *5* "pars bracket", cingulate sulcus, *6* precuneus, parietal lobe, *7* intraparietal sulcus, *8* interhemispheric fissure, *9* pars opercularis, inferior frontal lobe, frontal operculum, *10* Heschl's gyrus, *12* planum temporale, *14* head of the caudate nucleus, *15* thalamus, *16* internal capsule, *17* globus pallidus, putamen, claustrum (lentiform nucleus) *18* extreme capsule, *19* insula (anterior and posterior short insular gyri, anterior and posterior long insular gyri), *33* medial frontal gyrus, *34* superior temporal gyrus, *35*a posterior ascending ramus of the Sylvian fissure, *36* central sulcus of the insula

(anterior, medial and posterior short insular gyri divided, by the CS, from the anterior and posterior long insular gyri). The insula [19] is covered by the superior temporal gyrus [34], the frontal operculum [9] and the base of the sensorimotor strip. After identifying the anterior short gyrus of the anterior lobule of the insular cortex, on a transverse view, the anterior border between the insula and inferior frontal lobe is the anterior peri-insular sulcus. It abuts the insula [19], on one hand, and the pars opercularis [9] of the frontal operculum of the inferior frontal gyrus, on the other. The pars opercularis [9] has a triangular shape in axial sections and covers the anterior part of the insula [19]. It can be followed into the anterior cranial fossa where it abuts the gyrus orbitalis that runs parallel to the gyrus rectus. The convolution anterior to the pars opercularis [9] on the lateral surface is the pars triangularis [39], separated by the anterior ascending ramus [35d] of the Sylvian fissure.

2.1.3.2 Sagittal Sections

Beginning at the lateral border of the brain (in sagittal views, see Figs. 2.4 and 2.5) there is the Sylvian fissure [35b] that runs anterior-inferior to posterior-superior. Previously, the posterior margins have been described (see above). The Sylvian fissure separates the temporal lobe from the frontal lobe. At its anterior margin, it ascends into the anterior horizontal ramus [35c] and more dorsally into the anterior ascending ramus [35d] of the frontal operculum [9] that also overhangs the anterior aspect of the insula [19]. The anterior horizontal ramus [35c] separates the pars orbitalis [40] from the pars triangularis [39], whereas the anterior ascending ramus [35d] separates the pars triangularis [39] from the pars opercularis [9] of the frontal operculum of the inferior frontal gyrus that form an "M" (Naidich et al. 1995). The pars opercularis of the frontal operculum of the inferior frontal lobe harbours Broca's area. At its posterior margin, the pars opercularis is delimited by the anterior subcentral sulcus.

2.1.4 Auditory Cortex and Speech-Associated Temporoparietal Areas

2.1.4.1 Transverse Sections

From medial to lateral (see Figs. 2.5 and 2.6) towards the insula [19], the globus pallidus,

putamen and claustrum within the lentiform nucleus [17] can be differentiated. Between the lentiform nucleus [17] and the cortex of the insula [19] the extreme capsula [18] is depicted as a small rim of white matter. The Sylvian fissure [35b] separates the insula [19] from the temporal lobe. This is an easy definable landmark on axial views. The insula – taking anatomic variations into account – has 4–5 knobs (anterior, medial and posterior short insular gyri divided, by the CS [36], from the anterior and posterior long insular gyri). Posterior to the convolution that represents the section of the posterior long insular gyrus, a gyrus in the superior temporal lobe can be identified with a dorsomedial to anterior-lateral course, called the transverse temporal gyrus or Heschl's gyrus [10]. This is the primary auditory cortex (Mukamel et al. 2005; Devlin and Poldrack 2007). Number and size may vary (Penhune et al. 1996; Rademacher et al. 2001); however, this is another good landmark that is easy to define. Heschl's gyrus [10] might be interrupted by the sulcus intermedius of Beck. Two gyri on the right and only one on the left hemisphere can be found frequently (Shapleske et al. 1999). Heschl's sulcus [11], which borders Heschl's gyrus [10] posteriorly, is the anterior border of the planum temporale [12]. Although direct cortical stimulation intraoperatively may cause speech disturbances in this area (Sanai et al. 2008; Shapleske et al. 1999), the planum temporale [12] represents, more likely, the auditory association cortex. The planum temporale [12] extends on the superior surface of the temporal lobe and is delimited laterally by the superior temporal sulcus [13], posteriorly by the posterior ascending ramus and/or descending ramus of the Sylvian fissure and medially in the depth of the Sylvian fissure, which is less well defined (Shapleske et al. 1999). These borders are easier depicted in sagittal views; however, in transverse sections, remaining in the same plane in which Heschl's gyrus [10] can be found, the superior temporal sulcus [13] is the next biggest sulcus posterior to Heschl's sulcus [11]. Heschl's gyrus [10] bulges into the Sylvian fissure [35b]. The Sylvian fissure can therefore also be followed in ascending axial images. At the parietotemporal junction, sulci such as the Sylvian fissure or the superior temporal sulcus [13] ascend, whereas the sulcus intermedius primus descends. This hampers anatomical description in axial sections. Ascending in axial slice order, the superior temporal sulcus [13] diminishes. As Heschl's gyrus [10] bulges into the Sylvian fissure [35b], the Sylvian fissure can be followed on its course as posterior ascending ramus [35a] up to the level of the cella media of the lateral ventricles (in bicommissural orientation), as a big intersection posterior to Heschl's sulcus [11]. The posterior ascending ramus [35a] of the Sylvian fissure is imbedded in the supramarginal gyrus [37] which again is separated from the angular gyrus [38] by the sulcus intermedius primus. Descending in axial slice order, pre- and postcentral gyri can be identified as described above. The next sulcus dorsal to the postcentral sulcus is the intraparietal sulcus [7] which can be followed from the medial apical surface, laterally and dorsally in the parietal lobe [6]. Laterally, it ends above the sulcus intermedius primus and abuts the angular gyrus [38]. Size of the planum temporale [12] varies depending on sex, handedness and hemispherical dominance (Shapleske et al. 1999). Activation in functional imaging studies was found in verb generation tasks (Wise et al. 1991) and listening to tones, words and tone sequences (Binder et al. 1996, 1997, 2000).

2.1.4.2 Sagittal Sections

According to its dorsomedial to anterior-lateral course (see Fig. 2.6), the transverse temporal gyrus or Heschl's gyrus [10] abuts the base of the inferior sensorimotor strip (most likely the postcentral gyrus) at the lateral aspect and the posterior long gyrus of the insula [19] in more medially located sections. It is erected into the Sylvian fissure [35b]. Heschl's sulcus [11], which borders Heschl's gyrus [10] posteriorly, is the anterior border of the planum temporale [12]. The planum temporale [12] extends on the superior surface of the temporal lobe and is delimited laterally by the superior temporal sulcus [13], posteriorly by the posterior ascending ramus and/or descending ramus of the Sylvian fissure and medially in the depth of the Sylvian fissure, which is less well

defined (Shapleske et al. 1999). The Sylvian fissure can be followed from the anterior ascending [35d] and horizontal rami [35c] in the frontal operculum [9] of the inferior frontal gyrus, dorsally to the ascending [35a] and descending rami at the temporoparietal junction. Medially it is flanked by the insula [19], laterally by the superior temporal gyrus [34] and inferior parts of the pre- and postcentral gyri. Parallel to the Sylvian fissure [35b], the superior temporal gyrus [34] also demonstrates an anterior-posterior course. The posterior ascending ramus [35a] of the Sylvian fissure is imbedded in the supramarginal gyrus [37] which has a horseshoe appearance. Posterior to the supramarginal gyrus [37], the superior-inferior running sulcus intermedius primus separates it from the angular gyrus [38]. The superior temporal sulcus [13] ascends at its posterior end and diminishes.

2.1.4.3 Coronal Sections

In coronal views, the Sylvian fissure separating the temporal lobe from the insula and the frontal lobe can easily be seen. Originating from the temporal lobe, Heschl's gyrus points towards the insula (not shown).

2.1.5 Visual Cortex

2.1.5.1 Sagittal Sections

At the medial surface of the occipital lobe, there is a sulcus that zigzags anterior-posteriorly called the calcarine sulcus [27], along which the visual cortex is located. The calcarine sulcus [27] separates the superior lip from the inferior lip of the visual cortex.

References

Binder JR, Frost JA et al (1996) Function of the left planum temporale in auditory and linguistic processing. Brain 119:1239–1247

Binder JR, Frost JA et al (1997) Human brain language areas identified by functional imaging. J Neurosci 17:353–362

Binder JR, Frost JA et al (2000) Human temporal lobe activation by speech and nonspeech sounds. Cereb Cortex 10:512–528

Brandt T, Bartenstein P et al (1998) Reciprocal inhibitory visual-vestibular interactions: visual motion stimulation deactivates the parieto-insular vestibular cortex. Brain 121:1749–1758

Dechent P, Frahm J (2003) Functional somatotopy of finger representations in human primary motor cortex. Hum Brain Mapp 18:272–283

Devlin JT, Poldrack RA (2007) In praise of tedious anatomy. Neuroimage 37:1033–1041

Dronkers NF (1996) A new brain region for coordinating speech articulation. Nature 384:159–161

Ebeling U, Huber P et al (1986) Localization of the precentral gyrus in the computed tomogram and its clinical application. J Neurol 233(2):73–76

Eberstaller O (1890) Ein beitrag zur anatomie der oberfläche des grosshirns. Urban & Schwarzenberg, Wien/Leipzig

Fesl G, Moriggl B et al (2003) Inferior central sulcus: variations of anatomy and function on the example of the motor tongue area. Neuroimage 20(1):601–610

Kido DK, LeMay M et al (1980) Computed tomographic localization of the precentral gyrus. Radiology 135:373–377

Meyer JR, Roychowdhury S et al (1996) Location of the central sulcus via cor-tical thickness of the precentral and postcentral gyri on MR. AJNR Am J Neuroradiol 17(9):1699–1706

Mukamel R, Hagar G et al (2005) Coupling between neuronal firing, field potentials, and fMRI in human auditory cortex. Science 309:951–954

Nagao M, Takeda K et al (1999) Apraxia of speech associated with an infarct in the precentral gyrus of the insula. Neuroradiology 41:356–357

Naidich TP, Brightbill TC (1996) The pars marginalis: part I. A "bracket" sign for the central sulcus in axial plane CT and MRI. Int J Neuroradiol 2:3–19

Naidich TP, Valavanis AG et al (1995) Anatomic relationships along the low-middle convexity: part I – normal specimen and magnetic resonance imaging. Neurosurgery 36:517–532

Naidich TP, Kang E et al (2004) The insula: anatomic study and MR imaging display at 1.5 T. AJNR Am J Neuroradiol 25:222–232

Ojemann GA, Whitaker HA (1978a) The bilingual brain. Arch Neurol 35(7):409–412

Ojemann GA, Whitaker HA (1978b) Language localization and variability. Brain Lang 6(2):239–260

Ono M, Kubik S et al (eds) (1990) Atlas of the cerebral sulci. Georg Thieme, Stuttgart/New York

Oppenheimer S (1993) The anatomy and physiology of cortical mechanisms of cardiac control. Stroke 24:I3–I5

Overduin SA, Servos P (2004) Distributed digit somatotopy inprimary somatosensory cortex. Neuroimage 23(2):462–472

Penfield W, Rasmussen T (1950) The cerebral cortex in man. Macmillan, New York

Penhune VB, Zatorre RJ et al (1996) Interhemispheric anatomical differences in human primary auditory cortex: probabilistic mapping and volume measurement from magnetic resonance scans. Cereb Cortex 6:661–672

Price CJ (2000) The anatomy of language: contributions from functional neuroimaging. J Anat 197:335–359
Rademacher J, Galaburda AM et al (1992) Human cerebral cortex: localization, parcellation, and morphometry with magnetic resonance imaging. J Cogn Neurosci 4(4):352–374
Rademacher J, Morosan P et al (2001) Probabilistic mapping and volume measurement of human auditory cortex. Neuroimage 13:669–683
Riecker A, Ackermann H et al (2000) Opposite hemispheric lateralization effects during speaking and singing at motor cortex, insula and cerebellum. Neuroreport 11:1997–2000
Sanai N, Mirzadeh Z et al (2008) Functional outcome after language mapping for glioma resection. N Engl J Med 358(1):18–27
Shapleske J, Rossell SL et al (1999) The planum temporale: a systematic review of its structural, functional and clinical significance. Brain Res Rev 29:26–49
Wise R, Chollet U et al (1991) Distribution of cortical neuronal networks involved in word comprehension and word retrieval. Brain 114:1803–1817
Wise RJ, Greene J et al (1999) Brain regions involved in articulation. Lancet 353:1057–1061
Yousry TA, Schmid UD et al (1995) Topography of the cortical motor hand area: prospective study with functional MR imaging and direct motor mapping at surgery. Radiology 195(1):23–29
Yousry TA, Schmid UD et al (1997) Localization of the motor hand area to a knob on the precentral gyrus. A new landmark. Brain 120(Pt 1):141–157

Spatial Resolution of fMRI Techniques

3

Seong-Gi Kim, Tao Jin, and Mitsuhiro Fukuda

3.1 Introduction

Following its introduction over two decades ago, functional magnetic resonance imaging (fMRI) based on the blood oxygenation level-dependent (BOLD) contrast (Ogawa et al. 1990) has become the tool of choice for visualizing neural activity in the human brain. The conventional BOLD approach has been extensively used for pinpointing functional foci of vision, motor, language, and memory in normal and clinical patients. Intraoperative localization of functional foci will greatly improve surgical planning for epilepsy and tumor dissection, and potentially, for deep brain stimulation. Therefore, it is critical to understand the spatial resolution of fMRI relative to the actual neural active site (see review articles, (Kim and Ogawa 2002; Kim and Ugurbil 2003)).

In order to reliably determine the functional foci, high signal-to-noise ratio (SNR), which can be achieved using optimized imaging techniques, is critical. However, high SNR of fMRI techniques is not sufficient for high-resolution functional mapping if the signals that are being imaged do not have a high *specificity* to the local neural activity. Therefore, it is important to understand the signal source of BOLD fMRI and its fundamental limit of spatial resolution. Increased neural activity induces an increase in tissue metabolic demands. Thus, imaging the metabolic change (e.g., 2-fluorodeoxyglucose positron emission tomography) will yield high spatial specificity as metabolism will occur at the tissue at the site of the neuronal activity and not in the vasculature. Changes in neural activity and metabolism could directly or indirectly modulate the hemodynamic responses, including the cerebral blood flow (CBF), the cerebral blood volume (CBV), and the venous oxygenation levels. It has been well established that the magnitude of CBF change is well correlated with that of metabolic change. Thus, CBF mapping can pinpoint the most active spot of neural activity even if the exact spatial extent of the CBF response is controversial ((Malonek and Grinvald 1996) vs. (Duong et al. 2001)). The most commonly used BOLD technique is sensitive to paramagnetic deoxyhemoglobin (dHb), which is located at the capillaries and the venous draining vascular system (Ogawa et al. 1993), reducing spatial specificity of the gradient-echo BOLD signal. Often in fMRI studies, higher resolution BOLD images appear localized to large venous vessels because of larger contributions of venous signals due to the reduced volume fraction of tissue.

To understand the spatial resolution of hemodynamic responses, functional changes of different vascular origins should be carefully considered. In this chapter, we will discuss the intrinsic limitations and the improvements of spatial resolution.

S.-G. Kim (✉) • T. Jin • M. Fukuda
Department of Radiology, University of Pittsburgh,
3025 East Carson Street, Pittsburgh, PA 15203, USA
e-mail: kimsg@pitt.edu

S. Ulmer, O. Jansen (eds.), *fMRI – Basics and Clinical Applications*,
DOI 10.1007/978-3-642-34342-1_3,

3.2 Vascular Structure and Hemodynamic Response

As all fMRI signals originate from changes in hemodynamics, it is important to examine vascular structure. Detailed human brain vasculature was studied anatomically by Duvernoy et al. (1981). In short, vessels can be classified into pial and parenchymal vessels. Superficial pial arterial and venous vessels are numerous; arterial vessels with ~40–280-mm diameter have lesser branches than venous vessels with a ~130–380-mm diameter. These vessels can run a few centimeters and even longer. At the surface of the cortex, pial vessels connect to penetrating arteries and emerging veins at a right angle.

Parenchymal vessels can be divided into arteries, veins, and capillary network. Capillaries with ~5-μm average diameter and ~100-μm length are most abundant at the middle of the cortex (Pawlik et al. 1981). Intracortical arteries and veins can be further classified into their cortical depths (Duvernoy et al. 1981); group 1 and 2 vessels (with 10–20 μm diameter for arterial vessels and 20–30 μm for venous vessels) reach the upper cortical layers (layers 2–3), group 3 (with 15–30 μm for arterial vessels and 45 μm for venous vessels) the middle of the cortex (layers 3–5), group 4 (with 30–40 μm for arterial vessels and 65 μm for venous vessels) the lower cortical region (layer 6), and group 5 (with 30–75 μm for arterial vessels and 80–125 μm for venous vessels) the white matter. The number of intracortical arteries is ~4 times the number of intracortical veins (Duvernoy et al. 1981).

The intrinsic limit of spatial specificity of hemodynamic-based fMRI can be dependent on how finely CBF and CBV are regulated. Blood in each intracortical artery will supply a certain tissue volume, which is referred to as "the volume of arterial unit"; the volume of arterial unit is a volume with 0.33–0.5 mm diameter around a vessel for groups 2–3 and for 0.5–2 mm for group 5 (Duvernoy et al. 1981). If an individual intracortical artery can be independently regulated, spatial resolution can be 0.33–0.5 mm if arterial vessels or capillary changes are detected. Our fMRI studies suggest that intrinsic CBF and CBV changes are reasonably specific to submillimeter functional domains (Duong et al. 2001; Zhao et al. 2005), which are in the order of 0.5–0.7-mm diameter in cats. If the regulation point exists at precapillary arterioles or capillaries, then spatial resolution is even better. Recent papers indicate that precapillary arterioles indeed dilate during stimulation via astrocyte-capillary signaling (Zonta et al. 2003; Mulligan and MacVicar 2004; Metea and Newman 2006; Schummers et al. 2008; Petzold and Murthy 2011). In fact, the capillary network responds precisely in regions of neural activity in rat olfactory bulb, suggesting that spatial resolution of ~100 μm is achievable (Chaigneau et al. 2003).

When an imaging technique is sensitive to changes in intracortical veins, its spatial resolution is determined by the volume of tissue draining to each vein, which is considered to be "the volume of venous unit." The volume of venous units is a volume with 0.75–1 mm diameter around a vessel for groups 3–4 vessels and 1–4 mm diameter for group 5 (Duvernoy et al. 1981). Thus, spatial resolution cannot be better than 0.75 mm even if one single intracortical artery regulates precisely and downstream vessels respond. Intracortical venous vascular structures can be visualized with MRI. Figure 3.1 shows venographic images of cat brain, which were obtained using the BOLD contrast at 9.4 T. Venous vessels appear as dark lines or dots because venous blood has short T_2^* relative to tissue and arterial blood. Furthermore, blood susceptibility effect extends to tissue, enlarging apparent venous vessel size. Clearly, groups 3–5 intracortical veins can be easily visualized, and group 3 is most numerous. Typical distance between intercortical veins is ~0.5–1 mm (Fig. 3.1).

3.3 Spatial Resolution of BOLD fMRI

Since blood travels from capillaries to intracortical veins, and finally pial veins, a change in dHb concentration in blood can also occur far away from the actual gray matter region with increased neural activity, reducing effective spatial

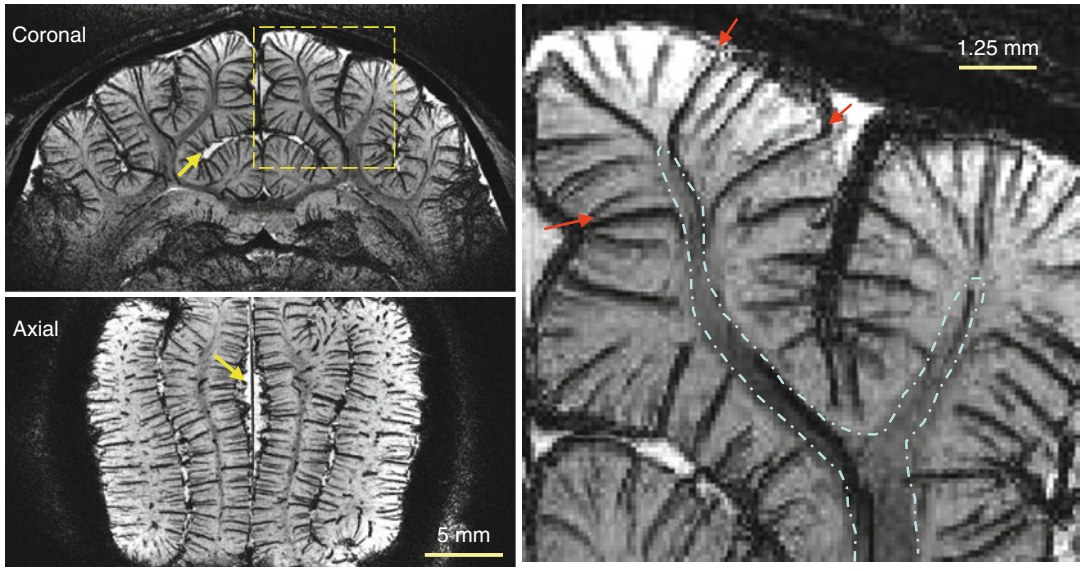

Fig. 3.1 Visualization of venous vessels in a cat brain. A 3-D T_2^*-weighted MR image was obtained at 9.4 T with 78 μm isotropic resolution and field of view of $2\times2\times4$ cm^3. A gradient-echo time of 20 ms was used to maximize the contrast between venous vessels and tissue. Data acquisition and processing methods were reported elsewhere (Park et al. 2008). 1.25-mm-thick slabs were selected, and minimum intensity projection was performed to enhance the contrast of venous vessels. As a surface coil was used, the ventral section in the coronal slice (*top left*) had poor signal-to-noise ratio (SNR), and thus, vessels could not be detected in that region. White matter areas (*contours in right*) can be distinguished from gray matter. *Dotted yellow box* in the coronal image was expanded 4 times into right. *Yellow arrows* cerebrospinal fluid (CSF) areas; *red arrows* venous vessels draining from white matter, which are "group 5." *Scale bar*, 5 mm for *left* and 1.25 mm for *right*

resolution. However, there is considerably more dilution of dHb change at farther downstream from the neuronally active region due to larger blood contribution from inactive regions. This dilution issue is also closely related to strength and spatial extent of neural activity. When the area of activation is small, this deoxygenated blood is diluted with blood from inactivated regions, effectively reducing the oxygenation level change. Thus BOLD fMRI is capable of differentiating small functional modules such as single whisker barrels (Yang et al. 1996). However, when the area of activation is large, blood drained from active regions can travel far away without much dilution.

Conventional BOLD response is related to a change in dHb contents within a voxel, thus directly correlated with (baseline dHb content) time (oxygenation change). Since a pixel with draining veins has high baseline dHb content, the BOLD response is particularly sensitive to large draining veins. Thus, spatial resolution of conventional BOLD signal can be much worse than that determined by the volume of venous unit. It is a reasonable assumption that conventional BOLD-based *high-resolution* fMRI may mostly detect the functionally less-specific large-vessel signals. To precisely localize functional foci, it is desirable to remove or minimize large-vessel contributions.

In order to understand which size of venous vessels can be detected by BOLD fMRI, we review the source of BOLD fMRI signals. Detailed biophysical models and explanations can be found in others (Ogawa et al. 1993; Weisskoff et al. 1994; Kim and Ugurbil 2003). The BOLD contrast induced by dHb arises from both intravascular (IV) and extravascular (EV) components. Since exchange of water between these two compartments (typical lifetime of the water in capillaries >500 ms) is relatively slow when compared with the imaging time (echo time <100 ms), MRI signals from these can be treated as separate pools.

The IV component is considered to be uniform within vessels because water rapidly exchanges between red blood cells (RBC) with paramagnetic dHb and plasma (average water residence time in RBCs = ~5 ms) and travels through space by exchange and diffusion. Thus, "dynamic" time averaging occurs over the many different fields induced by dHb. All water molecules inside the vessel will experience similar dynamic averaging, resulting in reduction of blood water T_2 in the venous pool. At high magnetic fields, venous blood T_2 can be shorter than tissue T_2 because R_2 ($=1/T_2$) of venous blood is quadratically dependent on magnetic field (Thulborn et al. 1982). Thus, at a higher magnetic field, IV contribution can be reduced by setting echo time much longer than blood T_2 (or T_2^*) (Lee et al. 1999; Jin et al. 2006). Alternatively, the IV signal can be reduced by applying bipolar gradients (as employed in diffusion-weighted images), which, with a "*b*" value of >30 s/mm^2, are expected to leave only the microvascular/extravascular contribution (Le Bihan et al. 1986).

The EV BOLD phenomenon has two biophysical sources (Ogawa et al. 1993; Weisskoff et al. 1994): one is due to intra-voxel dephasing of the magnetization in the presence of susceptibility-induced gradients, and the other is due to diffusion across the steep, susceptibility-induced gradients around small vessels (capillaries and venules). The first component induces high percentage signal changes around large venous vessels, regardless of magnetic field strength. Since field gradient decreases by $(r/a)^2$ where r is the distance from vessel to the region of interest and a is the vessel radius, the dephasing effect around a larger vessel is more spatially widespread. However, the dephasing effect of the static field can be refocused by the 180° radiofrequency (RF) pulse. Therefore, the EV contribution of large vessels can be reduced by using the spin-echo technique (which is similar to T_2-weighting in diagnostic imaging). The second component induces small signal changes in areas around capillaries and small venules. The reason is that tissue water around capillaries and small venules will be "dynamically" averaged over the many different fields during TE, similar to the IV component. This effect is larger at a higher magnetic field due to an increased susceptibility gradient within the water diffusion distance during TE. The dynamic diffusion-induced signals can be detected by either GE or SE approach. It is conceivable that the T_2-based BOLD technique is better localized to neuronal active region than T_2^*-based BOLD if the IV component of large vessels is removed (Zhao et al. 2004, 2006). However, the sensitivity of spin-echo techniques is less than gradient-echo BOLD signal.

To examine the spatial resolution of GE and SE BOLD fMRI, we used cortical layers as a model because layer 4 has the highest metabolic and CBF responses during neural activity as well as the highest synapse density and cytochrome oxidase activity (Woolsey et al. 1996). If the fMRI technique is highly specific to metabolic response and/or neural activity, the middle of the cortex should have the highest signal change. Figure 3.2 shows GE and SE BOLD fMRI maps of one isoflurane-anesthetized cat obtained during visual stimulation at 9.4 T (Zhao et al. 2006). To view the cortical cross section within a plane resolution of 156 × 156 μm^2, a 2-mm-thick imaging slice was selected perpendicular to the cortical surface. In both GE and SE BOLD maps, signal intensities increased during visual stimulation, indicating an increase in venous oxygenation. In conventional GE BOLD fMRI (Fig. 3.2), the highest percentage signal changes (yellow pixels) were seen in the CSF space (within the green contours), where pial veins are located. This large-vessel contribution to BOLD signals is reduced using the SE technique (Fig. 3.2) because the dephasing around large vessels refocuses. This result is consistent with high-field SE BOLD observations (Lee et al. 1999; Yacoub et al. 2003; Zhao et al. 2004).

SE BOLD fMRI is an excellent alternative approach if high spatial resolution is required and high magnetic field (such as 7 T) is available (Moon et al. 2007; Yacoub et al. 2008). Otherwise, conventional GE BOLD fMRI should be used with post-processing approaches to remove or minimize large-vessel contributions. Location of large pial venous vessels can be determined from

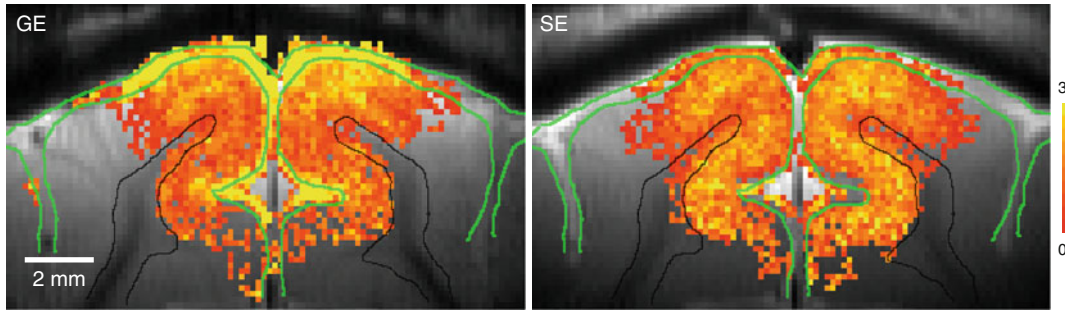

Fig. 3.2 High-resolution GE (*left*) and SE BOLD (*right*) fMRI maps of cat brain during visual stimulation overlaid on anatomical EPI images (Zhao et al. 2006). Coronal 2-mm-thick images with 156×156 μm² in-plane resolution were acquired using the four shot EPI technique at 9.4 T with gradient-echo time of 20 ms and spin-echo time of 40 ms. To determine statistically significant pixels, Student's *t* test was performed on a pixel-by-pixel basis with a t-value threshold of 2.0. Then, percentage signal changes were calculated for statistically active pixels. *Green contours* CSF area, *black contours* white matter, *scale bar* 2 mm, *color scale bar* 0.3–3 %

venographic images obtained with high-resolution T_2^*-weighted MR techniques (see Fig. 3.1) or from anatomical structures such as sulci and CSF. Large venous vessel areas tend to induce large BOLD percent change (see also Fig. 3.2) (Kim et al. 1994), delayed response (Lee et al. 1995), significant phase change (Menon 2002), and large baseline fluctuations (Kim et al. 1994). Although these criteria are subjective, they are effective in detecting and reducing large-vessel contamination.

3.4 Perfusion-Based fMRI Approaches

Alternative to the BOLD approach, CBF-weighted techniques which are sensitive mainly to parenchyma should be considered for mapping functional foci. CBF-weighted functional images can be obtained using MR by employing arterial blood water as an endogenous flow tracer. Arterial spin labeling (ASL) can be achieved by RF pulse(s). Then, labeled spins move into capillaries in the imaging slice and exchange with tissue water spins. To obtain only perfusion-related images, two images are acquired, one with ASL and the other without labeling. The difference between the two images is directly related to CBF, and relative CBF changes due to physiological perturbations can be measured. Most of the labeled water molecules extract into tissue and the remaining labeled water lose most of their labeling by the time they reach the draining veins due to its relatively short half-life (i.e., T_1 of blood). Thus, CBF-weighted MRI signals predominantly originate from tissue/capillary as well as arterial vessels (Ye et al. 1997; Lee et al. 2002; Kim and Kim 2005). Sensitivity of perfusion-weighted signals increases with magnetic field strength due to an increase in arterial blood T_1. ASL techniques include continuous ASL (Detre et al. 1992), flow-sensitive alternating inversion recovery (FAIR) (Kim 1995; Kwong et al. 1995), and various other techniques (Edelman et al. 1994; Wong et al. 1998).

Perfusion-based MR techniques have been used for fMRI studies. The spatial specificity of CBF-based fMRI is superior compared to GE BOLD techniques (Duong et al. 2001). Figure 3.3 shows BOLD and CBF functional maps during finger movements obtained at 4 T (Kim et al. 1997). The FAIR technique was used with inversion time of 1.4 s; the BOLD map was obtained from non-slice-selective inversion recovery images, while the CBF map was from subtraction of non-slice-selective from slice-selective inversion recovery images. Generally, activation areas are consistent between the maps measured by both techniques. However, pixel-wise comparison shows discrepancy between the two maps. Large signal changes in BOLD are located at draining veins indicated by arrows in the middle slice, while no signal change was observed in

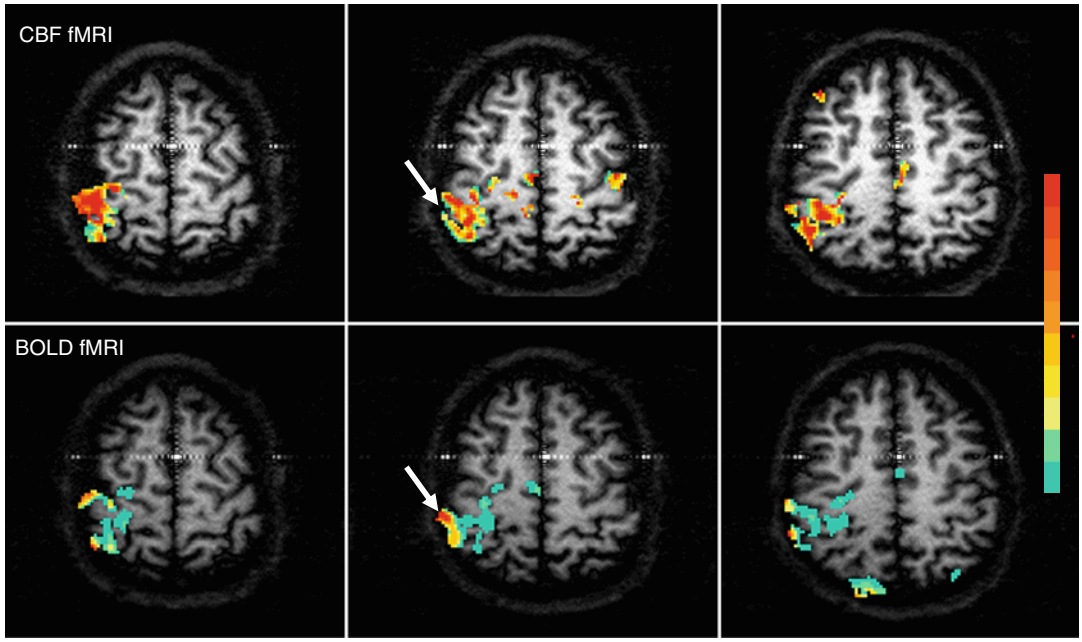

Fig. 3.3 BOLD and CBF functional maps of left-hand finger opposition, overlaid on T_1-weighted EPI (Kim et al. 1997). The flow-sensitive alternating inversion recovery (FAIR) technique was used to acquire BOLD (*bottom*) and CBF (*top*) contrast simultaneously at 4.0 T. BOLD maps were obtained from non-slice-selective inversion recovery (IR) images, while CBF maps were calculated from differences between slice-selective and non-slice-selective IR images. A cross-correlation value of 0.3 was used for threshold. For BOLD images, each color increment represents a 1 % increment starting from the bottom 1 %, while for CBF images, each color increment represents a 10 % increment starting from the bottom 10 %. The oblique arrow at the middle slice, indicating the right (contralateral) central sulcus, shows no activation in the CBF map, but large signal increase in the BOLD map, suggesting BOLD is sensitive to large draining veins

CBF. Tissue areas with high percent CBF changes have low BOLD signal changes. This indicates that the CBF approach is more specific to tissue than GE BOLD fMRI. To further confirm human fMRI results, BOLD and CBF fMRI were also compared in the cat's layer model. Figure 3.4 shows GE BOLD and CBF fMRI maps obtained during visual stimulation at 9.4 T (Jin and Kim 2008). CBF data were obtained using the FAIR technique with inversion time of 1.25 s, while gradient BOLD data were obtained with TE of 20 ms. The highest GE BOLD signal changes occur at the surface of the cortex, while the highest CBF changes occur at the middle of the cortex. This again demonstrates that perfusion-based fMRI technique is superior to GE BOLD for pinpointing functional foci precisely.

Proper CBF contrast is achieved only when enough time is allowed for the labeled arterial water to travel into the region of interest and exchange with tissue water. This makes it difficult to detect changes in CBF with a temporal resolution greater than T_1 of arterial blood water. Acquisition of a pair of images can further reduce temporal resolution and consequently SNR. Thus, it is difficult to obtain whole brain fMRI rapidly. However, baseline CBF value can be obtained, in addition to quantitative functional response. An additional advantage is less sensitivity to baseline signal drifts because slow non-activation-related signal changes can be removed by the pairwise subtraction (Kim 1995), and it is more stable to low-frequency stimulation compared to BOLD. Therefore, perfusion-based fMRI techniques are preferable for repetitive measurements over a long time period such as weeks and months, allowing investigations of functional reorganization and development. In

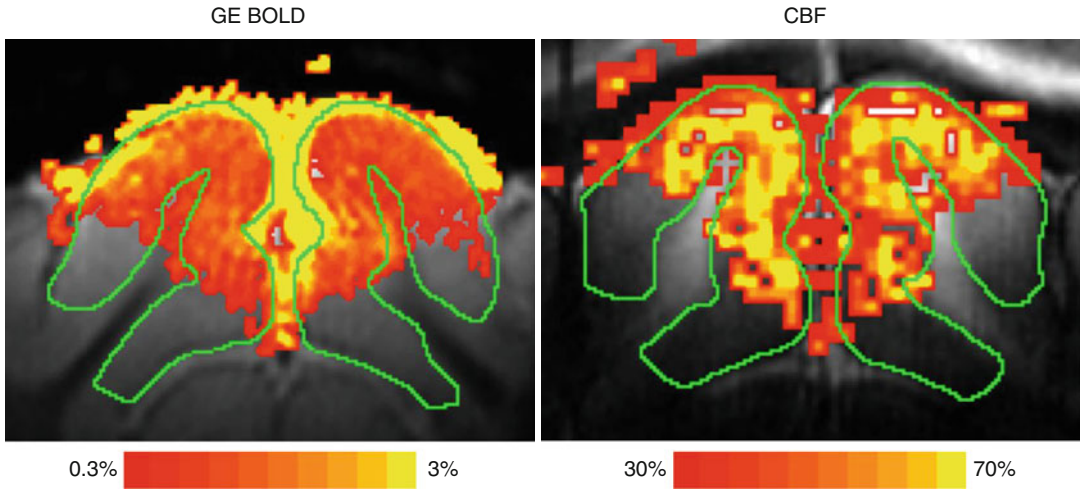

Fig. 3.4 BOLD and CBF fMRI maps of cat brain during visual stimulation overlaid on anatomical EPI images (Jin and Kim 2008). Coronal 2-mm-thick images with $312 \times 312\ \mu m^2$ in-plane resolution were acquired at 9.4 T; BOLD fMRI (*left*) was obtained with TE of 20 ms, while CBF (*right*) was detected with the FAIR technique with inversion time of 1.25 s. Maps were obtained by thresholding with a P value <0.05 and number of contiguous active pixels ≥3. The gray matter areas are outlined by *green contours*. The highest BOLD signal changes are observed at the surface of the cortex, while the highest CBF changes occur at the middle of the cortex. *Color bar* 0.3–3.0 % for BOLD and 30–70 % for CBF

clinical applications of fMRI where precise mapping is required around abnormal regions, the CBF-based fMRI technique is most appropriate because parenchymal signals are dominant.

Acknowledgments This work was supported in part by NIH (EB003324, EB003375, and NS44589). The authors thank their colleagues in the Neuroimaging Laboratory for providing the figures and for the discussion.

References

Chaigneau E, Oheim M et al (2003) Two-photon imaging of capillary blood flow in olfactory bulb glomeruli. Proc Natl Acad Sci USA 100(22):13081–13086

Detre JA, Leigh JS et al (1992) Perfusion imaging. Magn Reson Med 23:37–45

Duong TQ, Kim D-S et al (2001) Localized cerebral blood flow response at submillimeter columnar resolution. Proc Natl Acad Sci USA 98:10904–10909

Duvernoy HM, Delon S et al (1981) Cortical blood vessels of the human brain. Brain Res Bull 7(5):519–579

Edelman RR, Siewert B et al (1994) Qualitative mapping of cerebral blood flow and functional localization with echo-planar MR imaging and signal targeting with alternating radio frequency. Radiology 192:513–520

Jin T, Kim SG (2008) Cortical layer-dependent dynamic blood oxygenation, cerebral blood flow and cerebral blood volume responses during visual stimulation. Neuroimage 43(1):1–9

Jin T, Wang P et al (2006) Source of nonlinearity in echo-time-dependent BOLD fMRI. Magn Reson Med 55:1281–1290

Kim S-G (1995) Quantification of relative cerebral blood flow change by flow-sensitive alternating inversion recovery (FAIR) technique: application to functional mapping. Magn Reson Med 34:293–301

Kim T, Kim S-G (2005) Quantification of cerebral arterial blood volume and cerebral blood flow using MRI with modulation of tissue and vessel (MOTIVE) signals. Magn Reson Med 54:333–342

Kim S-G, Ogawa S (2002) Insights into new techniques for high resolution functional MRI. Curr Opin Neurobiol 12:607–615

Kim S-G, Ugurbil K (2003) High-resolution functional magnetic resonance imaging of the animal brain. Methods 30:28–41

Kim SG, Hendrich K et al (1994) Potential pitfalls of functional MRI using conventional gradient-recalled echo techniques. NMR Biomed 7(1–2):69–74

Kim S-G, Tsekos NV et al (1997) Multi-slice perfusion-based functional MRI using the FAIR technique: comparison of CBF and BOLD effects. NMR Biomed 10:191–196

Kwong KK, Chesler DA et al (1995) MR perfusion studies with T1-weighted echo planar imaging. Magn Reson Med 34:878–887

Le Bihan D, Breton E et al (1986) MR imaging of intravoxel incoherent motions: application to diffusion

and perfusion in neurologic disorders. Radiology 161:401–407
Lee AT, Glover GH et al (1995) Discrimination of large venous vessels in time-course spiral blood-oxygen-level-dependent magnetic resonance functional neuroimaging. Magn Reson Med 33:745–754
Lee S-P, Silva AC et al (1999) Diffusion-weighted spin-echo fMRI at 9.4 T: microvascular/tissue contribution to BOLD signal change. Magn Reson Med 42: 919–928
Lee S-P, Silva AC et al (2002) Comparison of diffusion-weighted high-resolution CBF and spin-echo BOLD fMRI at 9.4 T. Magn Reson Med 47:736–741
Malonek D, Grinvald A (1996) Interactions between electrical activity and cortical microcirculation revealed by imaging spectroscopy: implication for functional brain mapping. Science 272:551–554
Menon RS (2002) Postacquisition suppression of large-vessel BOLD signals in high-resolution fMRI. Magn Reson Med 47:1–9
Metea M, Newman E (2006) Glial cells dilate and constrict blood vessels: a mechanism of neurovascular coupling. J Neurosci 26:2862–2870
Moon CH, Fukuda M et al (2007) Neural interpretation of blood oxygenation level-dependent fMRI maps at submillimeter columnar resolution. J Neurosci 27: 6892–6902
Mulligan S, MacVicar B (2004) Calcium transients in astrocyte endfeet cause cerebrovascular constrictions. Nature 431:195–199
Ogawa S, Lee T-M et al (1990) Oxygenation-sensitive contrast in magnetic resonance image of rodent brain at high magnetic fields. Magn Reson Med 14:68–78
Ogawa S, Menon RS et al (1993) Functional brain mapping by blood oxygenation level-dependent contrast magnetic resonance imaging. A comparison of signal characteristics with a biophysical model. Biophys J 64(3):803–812
Park SH, Masamoto K et al (2008) Imaging brain vasculature with BOLD microscopy: MR detection limits determined by in vivo two-photon microscopy. Magn Reson Med 59:855–865
Pawlik G, Rackl A et al (1981) Quantitative capillary topography and blood flow in the cerebral cortex of cats: an in vivo microscopic study. Brain Res 208:35–58
Petzold GC, Murthy VN (2011) Role of astrocytes in neurovascular coupling. Neuron 71:782–797
Schummers J, Yu H et al (2008) Tuned responses of astrocytes and their influence on hemodynamic signals in the visual cortex. Science 320:1638–1643
Thulborn KR, Waterton JC et al (1982) Oxygenation dependence of the transverse relaxation time of water protons in whole blood at high field. Biochim Biophys Acta 714:265–270
Weisskoff RM, Zuo CS et al (1994) Microscopic susceptibility variation and transverse relaxation: theory and experiment. Magn Reson Med 31:601–610
Wong E, Buxton R et al (1998) Quantitative imaging of perfusion using a single subtraction (QUIPSS anf QUIPSS II). Magn Reson Med 39:702–708
Woolsey TA, Rovainen CM et al (1996) Neuronal units linked to microvascular modules in cerebral cortex: response elements for imaging the brain. Cereb Cortex 6:647–660
Yacoub E, Duong TQ et al (2003) Spin-echo fMRI in humans using high spatial resolutions and high magnetic fields. Magn Reson Med 49:655–664
Yacoub E, Harel N et al (2008) High-field fMRI unveils orientation columns in humans. Proc Natl Acad Sci USA 105:10607–10612
Yang X, Hyder F et al (1996) Activation of single whisker barrel in rat brain localized by functional magnetic resonance imaging. Proc Natl Acad Sci USA 93: 475–478
Ye FQ, Mattay VS et al (1997) Correction for vascular artifacts in cerebral blood flow values by using arterial spin tagging techniques. Magn Reson Med 37:226–235
Zhao F, Wang P et al (2004) Cortical depth-dependent gradient-echo and spin-echo BOLD fMRI at 9.4 T. Magn Reson Med 51:518–524
Zhao F, Wang P et al (2005) Spatial specificity of cerebral blood volume-weighted fMRI responses at columnar resolution. Neuroimage 27:416–424
Zhao F, Wang P et al (2006) Cortical layer-dependent BOLD and CBV responses measured by spin-echo and gradient-echo fMRI: insights into hemodynamic regulation. Neuroimage 30:1149–1160
Zonta M, Angulo MC et al (2003) Neuron-to-astrocyte signaling is central to the dynamic control of brain microcirculation. Nat Neurosci 6:43–50

The Electrophysiological Background of the fMRI Signal

4

Christoph Kayser and Nikos K. Logothetis

4.1 Introduction

The ability to non-invasively study the architecture and function of the human brain constitutes one of the most exciting cornerstones for modern medicine, psychology and neuroscience. Current in vivo imaging techniques not only provide clinically essential information and allow new forms of treatment but also reveal insights into the mechanisms behind brain function and malfunction. This supremacy of modern imaging rests on its ability to study the structural properties of the nervous system simultaneously with the functional changes related to neuronal activity. As a result, imaging allows us to combine information about the spatial organization and connectivity of the nervous system with information about the underlying neuronal processes and provides the only means to link perception and cognition with the neural substrates in the human brain. Functional imaging techniques build on the interconnections of cerebral blood flow (CBF), the brain's energy demand and the neuronal activity (for reviews on this topic, see Heeger and Ress 2002; Logothetis 2002; Logothetis and Wandell 2004; Lauritzen 2005). Indeed, elaborate mechanisms exist to couple changes in CBF and blood oxygenation to the maintenance and restoration of ionic gradients and the synthesis, transport and reuptake of neurotransmitters. More than 125 years ago, Angelo Mosso had already realized that there must be a relation between energy demand and CBF when he observed increasing brain pulsations in a patient with a permanent skull defect performing a mental task (Mosso 1881). Similar observations on the coupling of blood flow to neuronal activity (from experiments on animals) led Roy and Sherrington to make the insightful statement that "… the chemical products of cerebral metabolism contained in the lymph that bathes the walls of the arterioles of the brain can cause variations of the caliber of the cerebral vessels: that is, in this reaction, the brain possesses an intrinsic mechanism by which its vascular supply can be varied locally in correspondence with local variations of functional activity" (Roy and Sherrington 1890).

Nowadays, there is little doubt about the usefulness of imaging to basic research and clinical diagnosis. In fact, with the wide availability of magnetic resonance imaging (MRI), functional imaging has become a self-sustaining branch of neuroscience research. Yet, and despite all this progress, it is still not clear how faithfully functional imaging replicates the patterns of neuronal activity underlying the changes in brain perfusion. Debating over the spatial and temporal precision of the imaging signal, researchers have compared it to more direct measurements of electrical neuronal activity from electrophysiological approaches. This holds especially true for the blood-oxygenation level-dependent signal (BOLD-fMRI), which is probably the most widely

C. Kayser (✉) • N.K. Logothetis
Department Physiology of Cognitive Processes,
Max Planck Institute for Biological Cybernetics,
Spemannstrasse 38, Tübingen 72076, Germany
e-mail: christoph.kayser@tuebingen.mpg.de

S. Ulmer, O. Jansen (eds.), *fMRI – Basics and Clinical Applications*,
DOI 10.1007/978-3-642-34342-1_4,